Tailoring Yb^{3+} energy levels by local configuration of the garnet structure. The case of $Ca_3(NbGa□)_5O_{12}$ laser single crystal, a model for Yb:YAG

María Dolores Serrano, **Concepción Cascales**, **Carlos Zaldo***
Instituto de Ciencia de Materiales de Madrid. Consejo Superior de Investigaciones Científicas. c/ Sor Juana Inés de la Cruz 3. 28049 Madrid. Spain.
* Corresponding author Email: cezaldo@icmm.csic.es
Nicolas Trcera
Synchrotron Soleil, 91192 Gif-sur-Yvette Cedex, France
João Elias F. S. Rodrigues
Synchrotron ALBA. Carrer de la Llum 2, 26, Cerdanyola del Vallès, 08290 Barcelona. Spain.
Giulio Gorni
Instituto de Cerámica y Vidrio. Consejo Superior de Investigaciones Científicas. c/ Kelsen 5. 28049 Madrid. Spain
Mamoru Kitaura
Faculty of Science, Yamagata University, Yamagata, 990-8560, Japan
Hirokazu Masai
Department of Materials and Chemistry, National Institute of Advanced Industrial Science and Technology (AIST), Osaka, 563-8577, Japan

ELECTRONIC SUPPLEMENTARY INFORMATION

Index

ESI.1. Garnet composition guide for cationic substitutions.
ESI.2. Preparation of powdered polycrystalline CNGG garnets by Solid State Synthesis (SSS).
ESI.2.1. Mg-modified 8 at% Yb:CNGG.
ESI.2.2. Si-modified 8 at% Yb:CNGG.
ESI.2.3. Ge-modified 8 at% Yb:CNGG.
ESI.2.4. Ti-modified 8 at% Yb:CNGG.
ESI.2.5. V-modified 8 at% Yb:CNGG.
ESI.3. EDX characterization of 8 at% Yb:CNGG single crystals with different cationic modifications.
ESI.4. Preparation of XAS references.
ESI.4.1. Czochralski growth of $Ca_3Ga_2Ge_3O_{12}$ crystal as reference of 4-fold coordinated Ge^{4+}.
ESI.4.2. Spontaneous nucleation of α´-Ba_2TiO_4 as reference of 4-fold coordinated Ti^{4+}.
ESI.4.3. Spontaneous nucleation of Y_2TiMoO_8 as reference of 4-fold coordinated Ti^{4+}.
ESI.5. EXAFS results and data analysis.
ESI.6. Single crystal X-ray diffraction characterization.
ESI.6.1. scXRD of 30 at% Mg-modified 8 at% Yb:CNGG crystal.
ESI.6.2. scXRD of 20 at% Ge-modified 8 at% Yb:CNGG crystal.
ESI.6.3. scXRD of 10 at% Ti-modified 8 at% Yb:CNGG crystal.
ESI.7. Characterisation of 8 at% Yb:CNGG crystals grown in the composition limits for congruent melting.
ESI.8. Low temperature (T = 6 K) OA of Ge-, Si-, or V-modified 8 at% Yb:CNGG SSS products and single crystals.
ESI.8.1. Ge^{4+}.
ESI.8.2. Si^{4+}.
ESI.8.3. V^{5+}.

ESI.1. Garnet composition guide for cationic substitutions

(a)

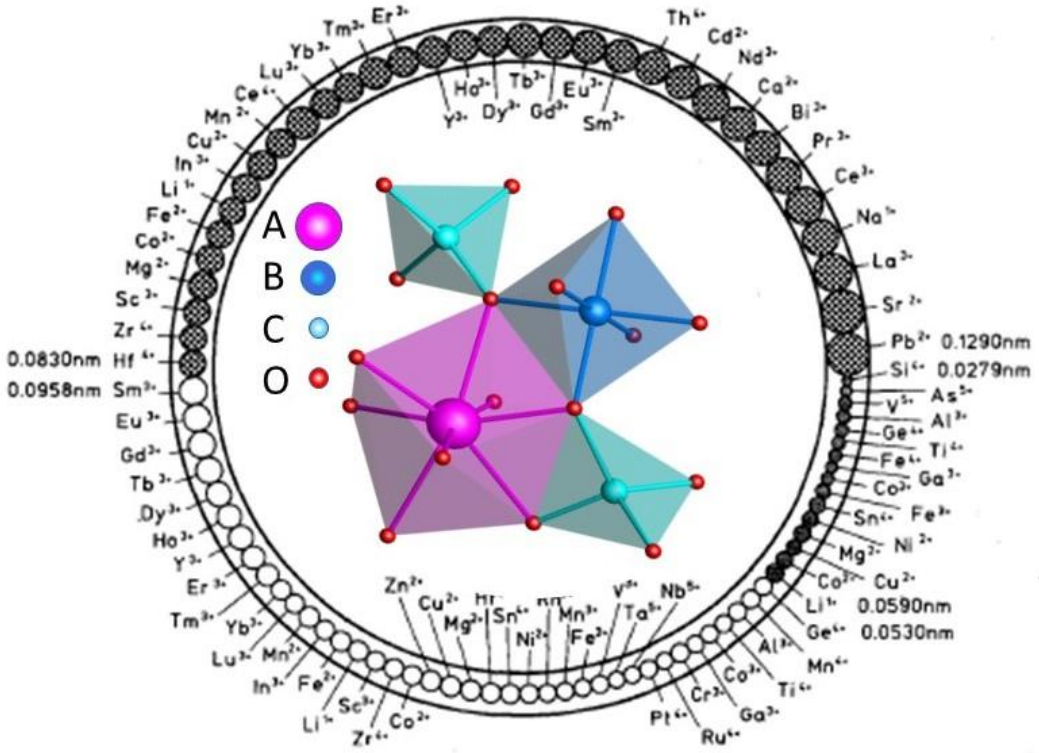

(b)

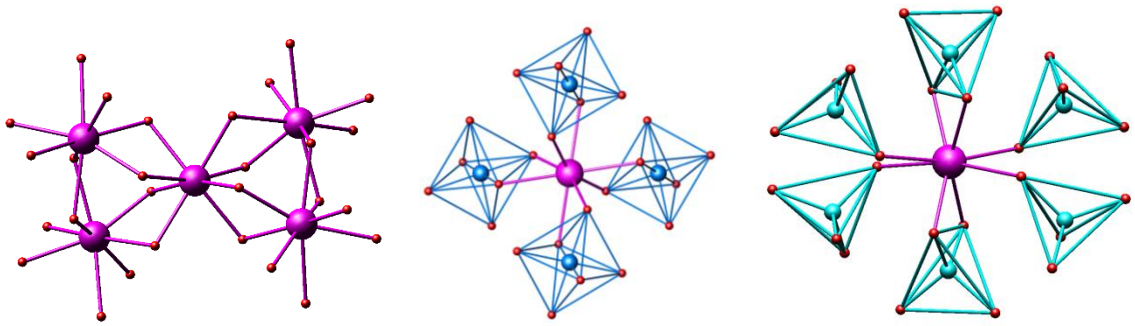

Figure ESI.1 Structural, compositional and coordination characteristics of garnet crystals. (a) Connection of oxygen polyhedra around the cationic positions and common cations found for the three garnet sites as a function of the ionic radius and oxidation state. Adapted with permission of Journal of Crystal Growth 102, 994, 1990, https://doi.org/10.1016/0022-0248(90)90870-Q. (b) First neighbour ionic distributions around the dodecahedral 24*c* site of the garnet crystalline structure: Left, coordination with other dodecahedral polyhedra. Centre, coordination with octahedral polyhedra. Right, coordination with tetrahedral polyhedra. O^{2-}, red spheres. Ca^{2+} and Yb^{3+}, violet spheres. 16*a* Nb^{5+} and Ga^{3+}, blue spheres. 24*d* Nb^{5+} and Ga^{3+}, cyan spheres.

Table.ESI.1. Ionic radius (r) mismatch (Δr) expected for hypothetical isovalent and heterovalent cationic substitutions in $Y_3Al_5O_{12}$ (YAG) and $Ca_3(NbGa\square)_5O_{12}$ (CNGG) garnets for possible coordination numbers (CN).

		YAG					CNGG				
Site	CN	Cation	r_1 (Å)	Cation	r_2 (Å)	Δr (%)	Cation	r_1 (Å)	Cation	r_2 (Å)	Δr (%)
24*c*	8	Y^{3+}	1.019	Sc^{3+}	0.87	-14.62	Ca^{2+}	1.12	K^{+}	1.51	+34.82
				Mg^{2+}	0.89	-12.66			Na^{+}	1.18	+5.36
				Lu^{3+}	0.977	-4.12			Bi^{3+}	1.17	+4.46
				Gd^{3+}	1.053	+3.33			Yb^{3+}	0.985	-12.05
									Te^{4+}	0.97	-13.39
									Mg^{2+}	0.89	-20.54
									Zr^{4+}	0.84	-25
									Hf^{4+}	0.83	-25.89
16*a*	6	Al^{3+}	0.535	Sc^{3+}	0.745	+39.25	Nb^{5+}	0.64	Sc^{3+}	0.745	+16,41
				Mg^{2+}	0.72	+34.58			Mg^{2+}	0.72	+12.5
				Ga^{3+}	0.62	+15.88			Hf^{4+}	0.71	+10.94
				Ti^{4+}	0.605	+13.08			Ga^{3+}	0.62	-3.12
				Mo^{6+}	0.59	+10.28			Ti^{4+}	0.605	-5.47
				V^{5+}	0.54	+9.35			Mo^{6+}	0.59	-7.81
				Ge^{4+}	0.53	-0.93			Te^{6+}	0.56	-12.5
				Si^{4+}	0.4	-25.23			V^{5+}	0.54	-15.62
									Ge^{4+}	0.53	-17.19
									Si^{4+}	0.4	-37.5
24*d*	4	Al^{3+}	0.39	Li^{+}	0.59	+51.28	Ga^{3+}	0.47	Li^{+}	0.59	+25.53
				Mg^{2+}	0.57	+46.15			Mg^{2+}	0.57	+21.27
				Ga^{3+}	0.47	+20.51			Nb^{5+}	0.48	+2.13
				Ti^{4+}	0.42	+7.69			Te^{6+}	0.43	-8.51
				Mo^{6+}	0.41	+5.13			Ti^{4+}	0.42	-10.64
				Ge^{4+}	0.39	0			Mo^{6+}	0.41	-12.76
				V^{5+}	0.355	-8.97			Ge^{4+}	0.39	-17.02
				Si^{4+}	0.26	-33.33			V^{5+}	0.355	-24.47
									Si^{4+}	0.26	-44.68

Table ESI. 2. Summary of radial interionic distances and coordination number, CN, for 24*c*, 16*a* and 24*d* sites of CNGG garnets and those obtained from the EXAFS analyses (bold italic cases). The unit cell lattice parameter, *a*, of each used crystal is also indicated.

Central cation	Neighbours	CN	Interionic distance (Å)							
			Undoped	8 at% Yb	30 at% Mg+8 at% Yb		20 at% Ge+8 at% Yb		10 at% Ti+8 at% Yb	
			a= 12.4969 Å	*a*= 12.4728 Å	*a*= 12.4892 Å		*a*= 12.4159 Å		*a*= 12.4720 Å	
4*c* (Ca)	96*h* (O)	4	2.412(1)	2.403(1)	2.405(2)		2.394(1)		2.4054(9)	
	96*h* (O)	4	2.539(1)	2.532(1)	2.533(2)		2.519(1)		2.5281(9)	
	24*d* (Ga2)	2	3.1242	3.1181	3.1223		3.1041		3.1180	
	16*a* (Nb1)	4	3.4930	3.4862	3.4908		3.4705		3.4860	
	24*c* (Ca)	4	3.8264	3.8190	3.8240		3.8018		3.8188	
	24*d* (Ga2)	4	3.8264	3.8190	3.8240		3.8018		3.8188	
	96*h* (O)	4	3.965(1)	3.964(1)	3.969(2)		3.947(1)		2.9638(9)	
16*a* (Nb1)	96*h* (O)	6	1.986(1)	1.991(1)	1.984(2)		1.991(1)		1.9882(9)	***1.96(2)***
	24*c* (Ca)	6	3.4930	3.4862	3.4908		3.4705		3.4860	***3.41(4)***
	24*d* (Ga2)	6	3.4930	3.4862	3.4908		3.4705		3.4860	***3.44(3)***
	96*h* (O)	6	3.920(1)	3.909(1)	3.922(2)		3.882(1)		3.9087(9)	
24d (Ga2)	96*h* (O)	4	1.850(1)	1.844(1)	1.856(2)	***1.93(2)***	1.827(1)	***1.79(2)***	1.8472(9)	
	24*c* (Ca)	2	3.1242	3.1181	3.1223		3.1041	***3.08(2)***	3.1180	
	96*h* (O)	4	3.432(1)	3.431(1)	3.436(2)		3.413(1)		3.4280(9)	
	16*a* (Nb1)	4	3.4930	3.4862	3.4908		3.4705	***3.41(5)***	3.4860	
	96*h* (O)	4	3.784(1)	3.781(1)	3.784(2)		3.761(1)		3.7833(9)	
	96*h* (O)	4	3.801(1)	3.785(1)	3.796(2)		3.768(1)		3.7853(9)	
	24*d* (Ga2)	4	3.8264	3.8190	3.8240		3.8018	***3.75(5)***	3.8188	
	24*c* (Ca)	4	3.8264	3.8190	3.8240		3.8018	***3.85(7)***	3.8188	

ESI.2. Preparation of powdered polycrystalline CNGG garnets by Solid State Synthesis (SSS)

As starting materials for crystal growth, we used CNGG powders obtained by solid state synthesis (SSS) heating precursor powders until foreign phases were fully eliminated or their contribution minimised, see the following sections. Ultrahigh purity (≥99.99 %) precursor powders of $CaCO_3$ (Alfa Aesar), Nb_2O_5 (Aldrich), Ga_2O_3 (Aldrich), Yb_2O_3 (acquired through Shanghai Zimei International Co ltd) and corresponding modifiers: Li_2CO_3 (99.997 % Alfa Aesar), MgO (97 % Merck), SiO_2 (99.999 % Alfa Aesar), TiO_2-rutile (99+ % Alfa Aesar), GeO_2(99.99 % Aldrich), NH_4VO_3(99.0 % Sigma Aldrich) and MoO_3 (99.5 % Alfa Aesar) were used. The precursor powders were mixed in the required compositions and heated firstly for 6 h to 800 ºC to decompose $CaCO_3$. The minimum temperature required to form the garnet phase was determined by 24 h annealing in the 1270-1330 ºC temperature range. This annealing was repeated several times with intermediate grinding of the products, increasing the temperature by 10 ºC in each heating cycle until the garnet phase was the only one present. In the following sections it is shown in detail that despite the repeated annealings, the coexistence of minor contributions of non-garnet phases is unavoidable for Mg-, Si-, and Ge-modified SSS powders, even at the lowest substitution level studied (5 at%), see in ESI sections ESI.2.1-ESI.2.2, and ESI.2.3. For For Ti-modified CNGG SSS powders, non-garnet phases appear only for >20 at% Ti substitution; see in ESI section ESI.2.4. For V-modified 8 at% Yb:CNGG SSS (1250 ºC / 37 h) powders, the non-garnet phases were found for V concentrations larger than 10 at% of the 24*d* tetrahedral occupancy, see in ESI section ESI.2.5.

ESI.2.1. Mg-modified 8 at% Yb:CNGG

The formation of the garnet phase by SSS from $MgO/Yb_2O_3/CaCO_3/Nb_2O_5/Ga_2O_3$ precursor mixtures was studied by XRD. An extra amount of MgO is added to the Yb:CNGG composition taking Nb as reference. The mixtures were annealed at 1335 ºC for 12 h. Figure ESI.2a shows that although the CNGG garnet phase is well formed for all Mg compositions studied, residual non-garnet phases coexist with it even at the lowest Mg composition synthesised (5 at% Mg).

For the growth of Mg-modified 8 at% Yb:CNGG crystals, the starting Yb doped CNGG pure garnet was first prepared by SSS carried out in two stages: First, the powder was heated up to 1000 ºC for 6 hours, ground, and then heated again at 1400 ºC for 12 hours. This 8 at% Yb:CNGG garnet was mixed prior to melt with the desired amount of MgO powder taken as reference Nb composition. Crystals with two Mg concentrations, namely 7.35 at% Mg and 30 at% Mg extra to the Nb content, were grown. Figure ESI.2b shows that the crystals obtained by this method only contain the garnet phase and X-ray fluorescence evaluations; see in ESI Figure ESI.7b shows the Mg incorporation into the crystal.

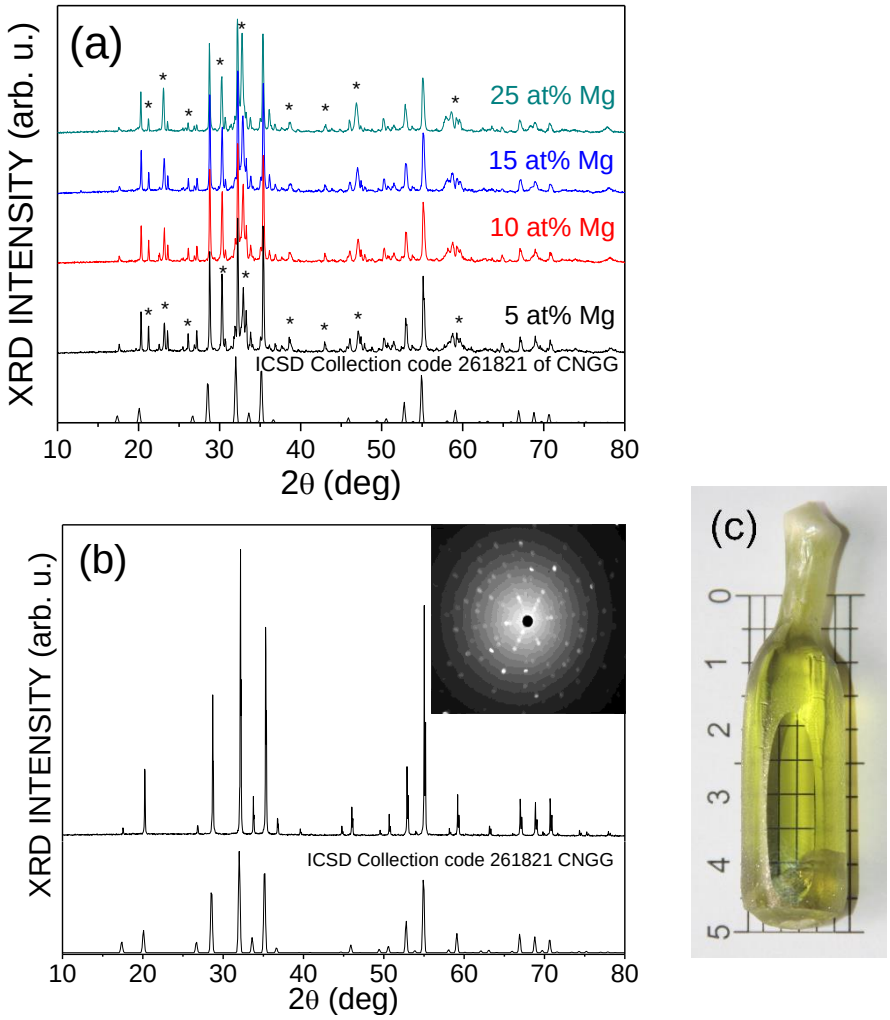

Figure ESI.2. (a) Room temperature X-ray diffraction (XRD) scans of Mg-modified 8 at% Yb:CNGG SSS polycrystalline products obtained from precursor mixtures of oxides heated to 1335 ºC for 12 h. * symbols label non-garnet XRD peaks. (b) XRD scan of powdered 30 at% Mg-modified 8 at% Yb:CNGG single crystal. The inset shows a 110 Laue pattern of this crystal. The bottom panels in a) and b) show the angular 2θ positions of the XR reflections corresponding to the CNGG garnet phase as given by the 261821 file of the ICSD database. (c) Image of the 2-side polished grown 30 at% Mg-modified 8 at% Yb:CNGG single crystal. The scale is in cm.

ESI.2.2. Si-modified 8 at% Yb:CNGG

The products for the preliminary study of the Si incorporation into Yb:CNGG were prepared by SSS using two different mixtures. In all cases the Si composition was discounted from the Ga one. Precursor preliminary phase evaluation and subsequent crystal growth were performed using $SiO_2/Yb_2O_3/CaCO_3/Nb_2O_5/Ga_2O_3$ mixtures by annealing them first at 900 ºC for 6 h followed by grinding and further annealing at 1320 ºC for 12 h. Figure ESI.3a shows the results obtained in this way. Although the polycrystalline CNGG garnet phase is always observed, even for the lowest 10 at% of Si doping, some additional non-garnet X-ray reflections show the coexistence of another phase. The latter is even more evident as the Si concentration increases to 20 at%.

As an attempt to avoid the presence of this non-garnet phase, a $SiO_2/C_6H_9O_6Yb\text{-}xH_2O/CaCO_3/C_4H_4NNbO_9\text{-}xH_2O/Ga_2O_3$ (oxide-acetate-ammonium) mixture was annealed at 800 ºC for 8 h, ground, and further heated at 1290 ºC for 12 h. Figure ESI.3.b shows the results obtained. Again, foreign phases are observed even at the smallest amount of 5 at% Si tested.

Despite the possible coexistence of non-garnet phases in the melt, the crystal growth of 5 at%, 10 at% and 20 at% Si-modified 8 at% Yb:CNGG was attempted. Crystals with poor optical quality were obtained in all these cases. Although EDX results show the presence of Si in the solidified material, see in ESI Figure ESI.7e, the local microscopic composition determined by EPMA shows large dispersion. Some crystal areas are Ga-rich and Si is confined to specific locations. On the other hand, the XRD scan of the powdered 20 at% Si-modified 8 at% Yb:CNGG crystal shown in Figure ESI.3c contains some non-garnet peaks. Thus, the solidified material seems to be a tweening of the garnet CNGG with some other phases. The contribution of these non-garnet phases is also observed in the spectroscopic studies presented later in section ESI.8.2.

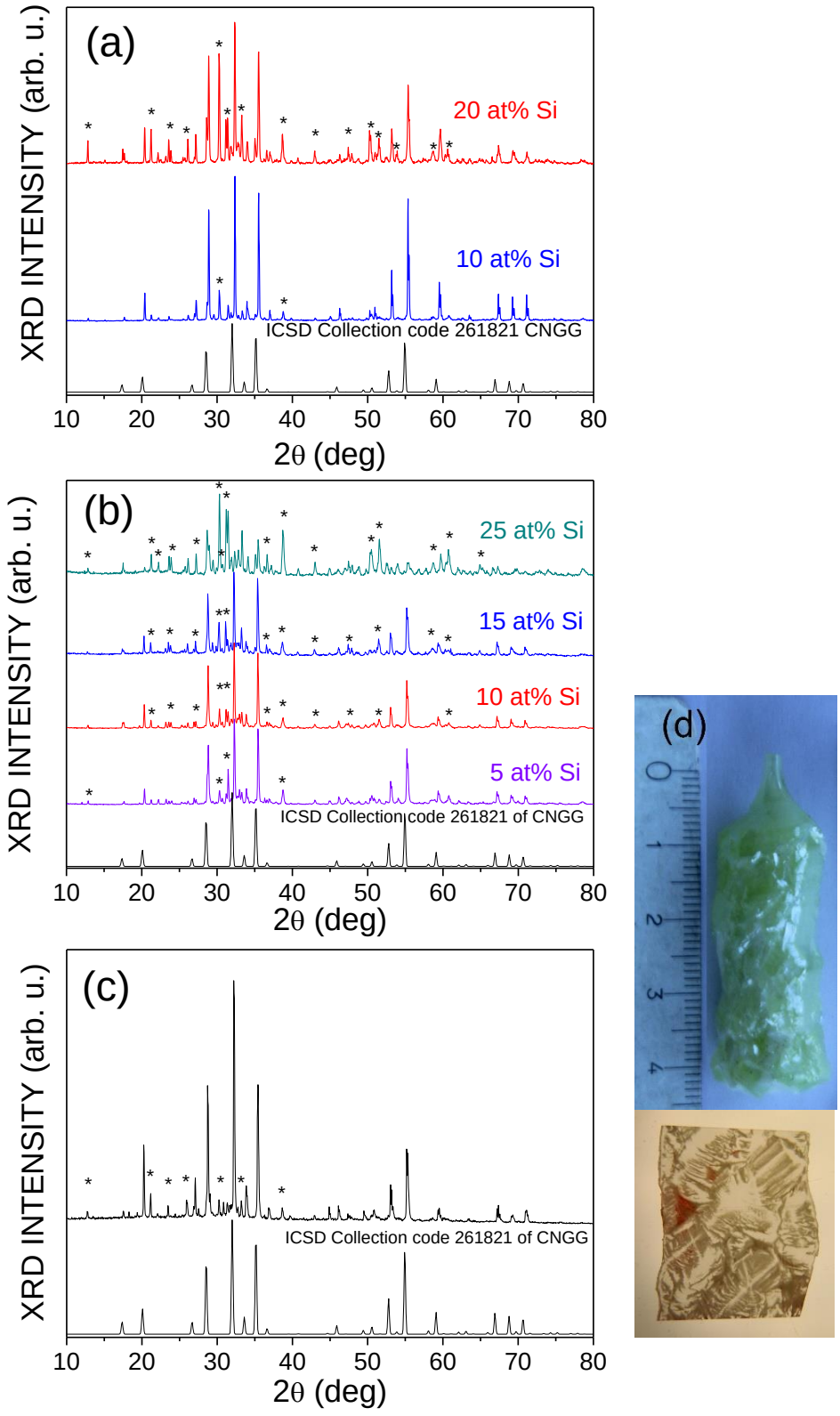

Figure ESI.3. Room temperature X-ray diffraction (XRD) scans of Si-modified 8 at% Yb:CNGG products. (a) Products obtained by SSS from oxides. (b) Products obtained by SSS using acetate-ammonium precursors. (c) Powdered 20 at% Si-modified 8 at% Yb:CNGG solidified material. * symbols label non-garnet peaks. The bottom panels in a), b) and c) show the angular 2θ positions of the XR reflections corresponding to the CNGG garnet phase as given by the 261821 file of the ICSD database. (d) Image of the as-grown solidified material and of a polished section.

ESI.2.3. Ge-modified 8 at% Yb:CNGG

Preliminary studies of the formation of the garnet phase in the Ge-modified 8 at% Yb:CNGG system were made by SSS of $GeO_2/Yb_2O_3/CaCO_3/Nb_2O_5/Ga_2O_3$ precursor mixtures by annealing at 1335 ºC for 12 h. Figure ESI.4a shows that the garnet peaks are observed for all tested Ge compositions up to 25 at% Ge discounted of total Nb^{5+} and Ga^{3+} compositions. Although minor contributions of non-garnet phases were always present, $Ca_3Nb_{1.0833}Ga_{2.8834}Ge_{0.9083}O_{12}$ and $Ca_{2.76}Yb_{0.24}Nb_{1.0833}Ga_{2.8834}Ge_{0.9083}O_{12}$ compositions (≈20 at% Ge substituting the total Nb and Ga content) were first synthesised by SSS and later grown by the Czochralski method. The Ge crystal composition determined by EMPA shows that up to 8 at% of the total Nb and Ga sites are occupied by Ge. Figure ESI.4b shows the powder XRD scan of the 20 at% Ge-modified 8 at% Yb:CNGG crystal. Only the CNGG garnet phase is observed.

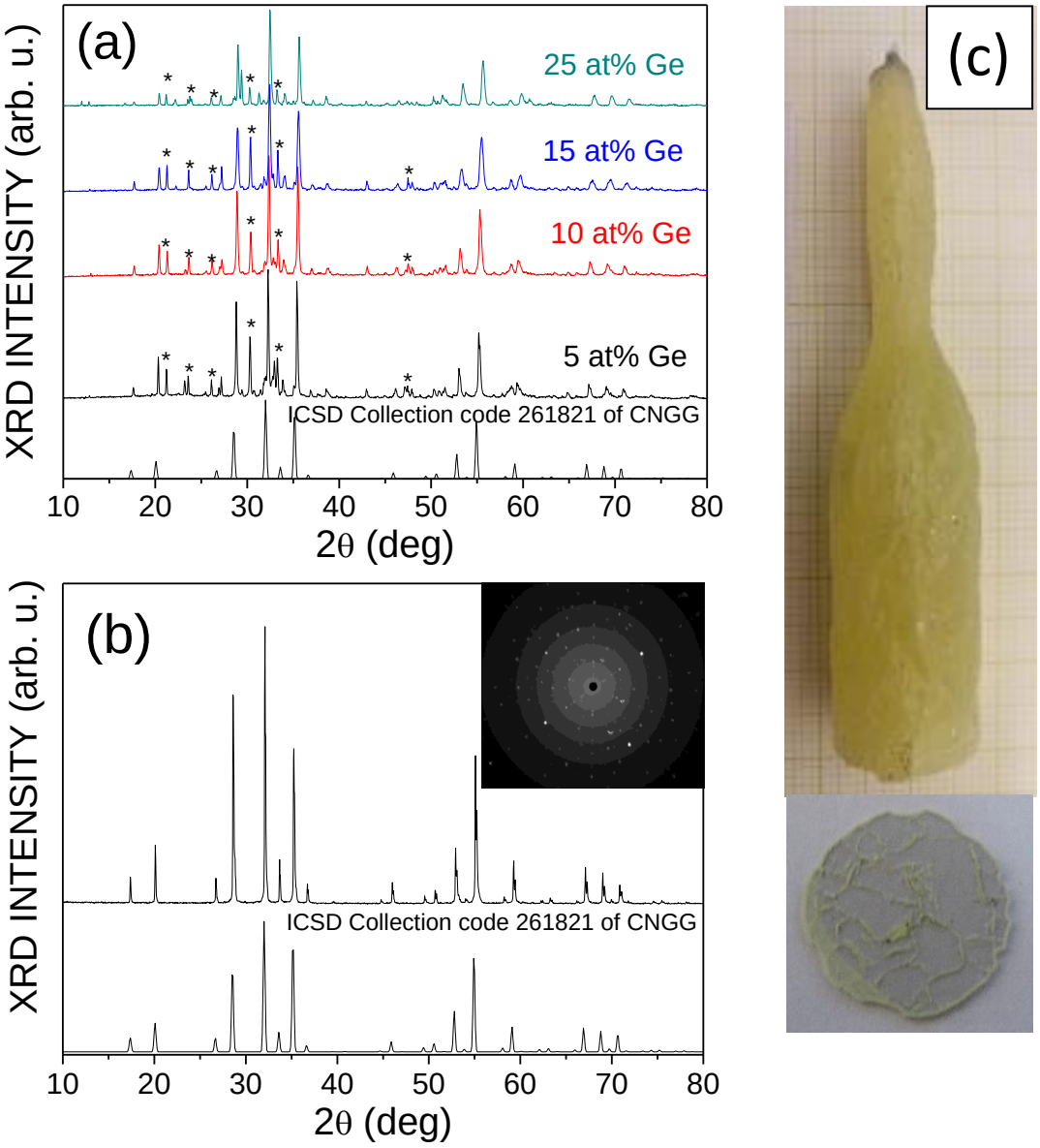

Figure ESI.4. Room temperature powder X-ray diffraction (XRD) scans of (a) Ge-modified 8 at% Yb:CNGG SSS products and (b) 20 at% Ge-modified 8 at% Yb:CNGG single crystal. The inset shows a 110 Laue pattern of this crystal. * symbols label non-garnet XRD peaks. The bottom panels in a) and b) show the angular 2θ positions of the XR reflections corresponding to the CNGG garnet phase as given by the 261821 file of the ICSD database. (c) Image of the 20 at% Ge-modified 8 at% Yb:CNGG grown single crystal and of a two-side polished cross-section. The small square scale is 1x1 mm.

ESI.2.4. Ti-modified 8 at% Yb:CNGG

Figure ESI.5a shows the powder XRD scans of the SSS products of 8 at% Yb:CNGG modified with increasing amounts of Ti^{4+} in substitution of Nb^{5+}. The products were prepared by SSS by a first annealing of 24 h at 1000 ºC followed by regrind and new annealing of 24 h at 1150 ºC. For Ti compositions above 15 at% some X-ray reflections not corresponding to the garnet phase are observed and labeled (*) in the figure. These results suggest that 15-20 at% substitution of Nb is the upper limit to achieve single crystals with the CNGG garnet phase. 8 at% Yb:CNGG crystals grown with a 10 at% substitution of Nb exclusively show the garnet phase; see Figure ESI.5b.

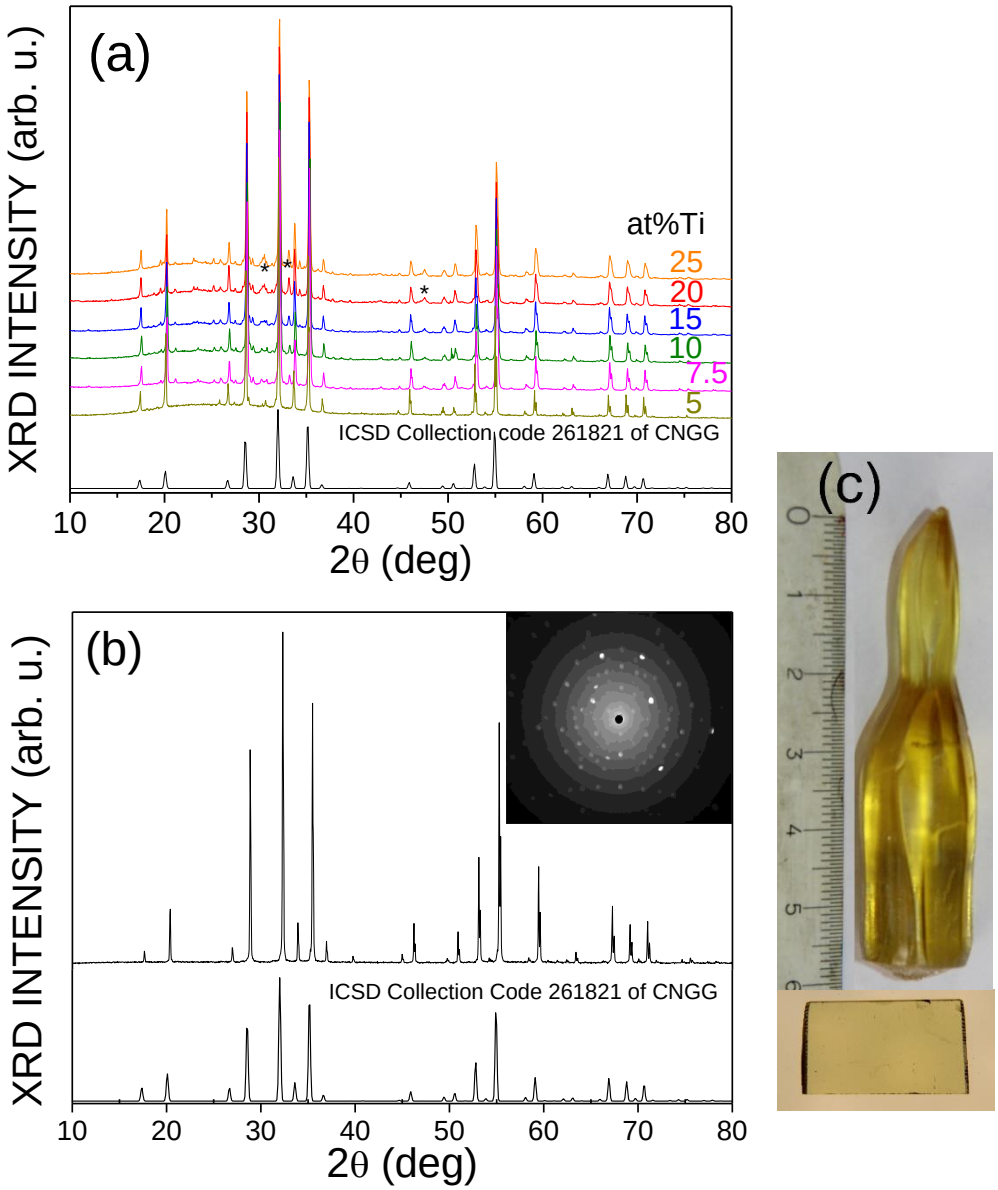

Figure ESI.5. (a) Room temperature powder X-ray diffraction (XRD) scans of 8 at% Yb:CNGG SSS polycrystalline products modified with increasing amounts of Ti^{4+} in substitution of Nb^{5+}. * symbols label non-garnet XRD peaks. (b) XRD scan of a powdered 10 at% Ti-modified 8 at% Yb:CNGG crystal. The inset shows a 111 Laue pattern of this crystal. The bottom panels in a) and b) show the angular 2θ positions of the XR reflections corresponding to the CNGG garnet phase as given by the 261821 file of the ICSD database. (c) Image of the as-grown 10 at% Ti-modified 8 at% Yb:CNGG single crystal (the scale is in cm) and of a two-side polished cross-section.

ESI.2.5. V-modified 8 at% Yb:CNGG

Polycrystalline samples of 8 at% Yb:CNGG modified with increasing amounts (5, 10, 15 and 25 at%) of V^{5+} over tetrahedral 24*d* sites of the cubic garnet structure were prepared by SSS. For each composition, stoichiometric required amounts of the starting reagents, $CaCO_3$ (Alfa Aesar, 99.5%), Ga_2O_3 (Cerac, 99.999%), Nb_2O_5 (Sigma Aldrich, 99.9%), Yb_2O_3 (acquired through Shanghai Zimei International Co Ltd, 99.99%), and NH_4VO_3 (Sigma Aldrich ≥ 99.0%), were mixed and heated in platinum crucibles, firstly 6 h to 800 ºC for $CaCO_3$ decomposition, and later up to 1250 ºC during 37 h, with intermediate regrindings. The XRD of the resulting powders is shown in Figure ESI.6. Up to 10 at% of V content, only the garnet phase is observed. At 15 at% V and above, additional non-garnet XRD peaks are observed.

These results motivated the growth of 10 at% V-modified 8 at% Yb:CNGG single crystals. Although XRD of this crystal shows the pure garnet phase, EDX (Figure ESI.7f) and EMPA results indicated that vanadium was not incorporated in the single crystal solid phase in any measurable amount.

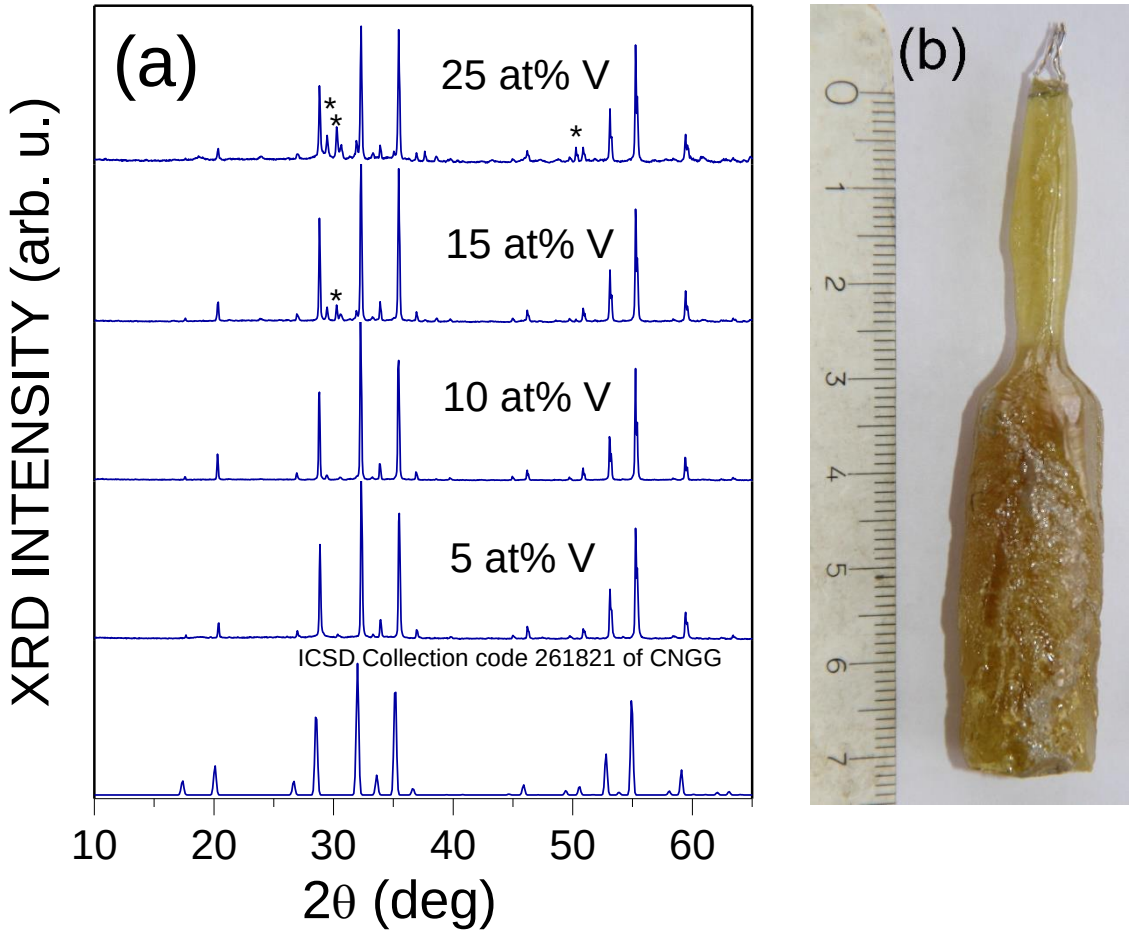

Figure ESI.6. Room temperature X-ray diffraction (XRD) scans of 8 at% Yb:CNGG polycrystalline products with increasing amounts of V^{5+} over tetrahedral 24*d* sites of the cubic garnet structure. * symbols label non-garnet XRD peaks. The bottom panel in a) shows the angular 2θ positions of the XR reflections corresponding to the CNGG garnet phase as given by the 261821 file of the ICSD database. (c) Image of the 10 at% V-modified 8 at% Yb:CNGG solidified material (the scale is in cm).

ESI.3. EDX characterization of 8 at% Yb:CNGG single crystals with different cationic modifications

(a) 8 at% Yb:CNGG

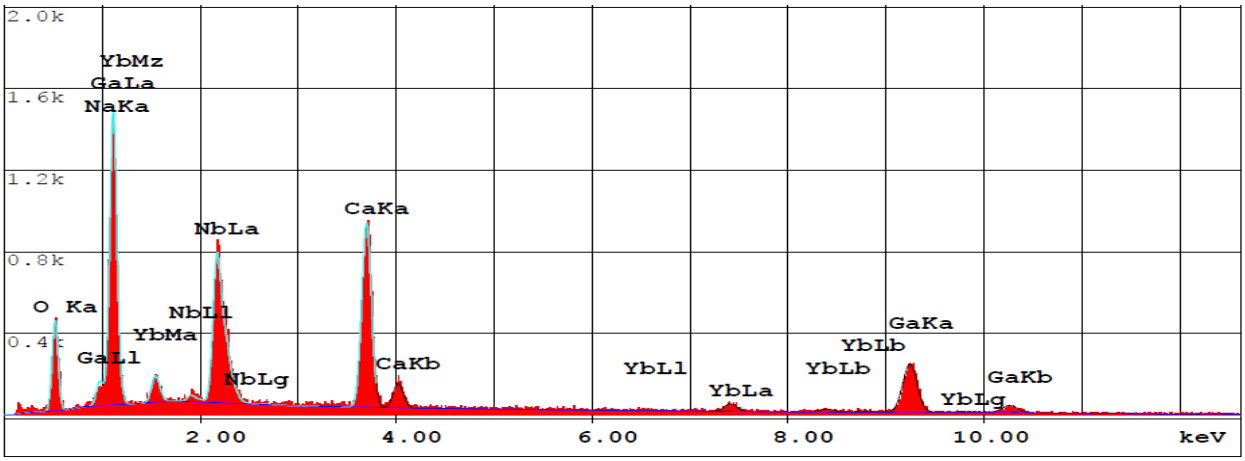

(b) 30 at% Mg-modified 8 at% Yb:CNGG

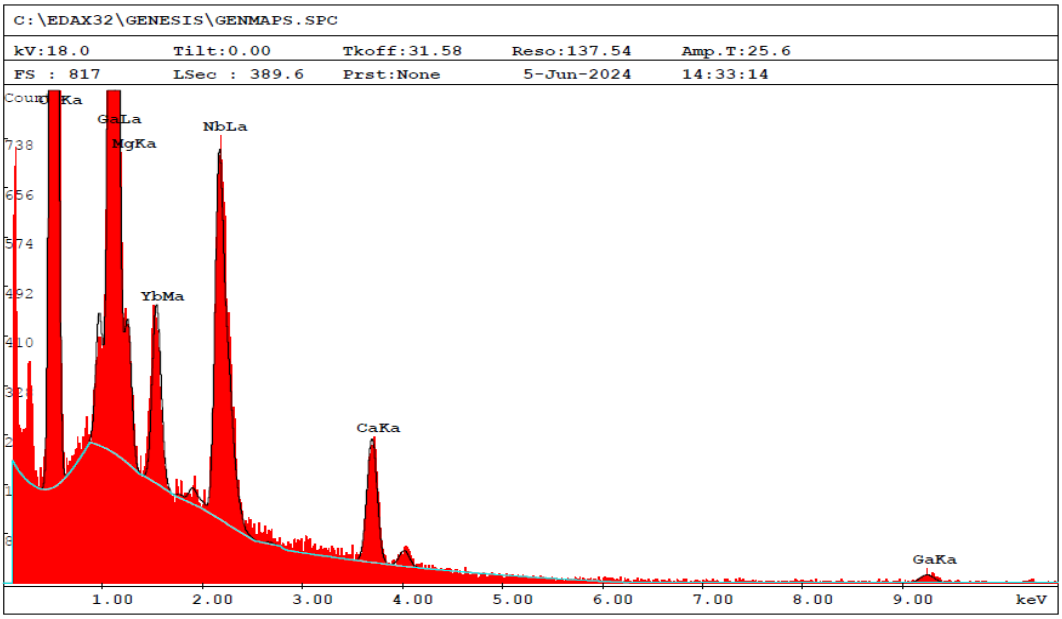

(c) 20 at% Ge-modified 8 at% Yb:CNGG

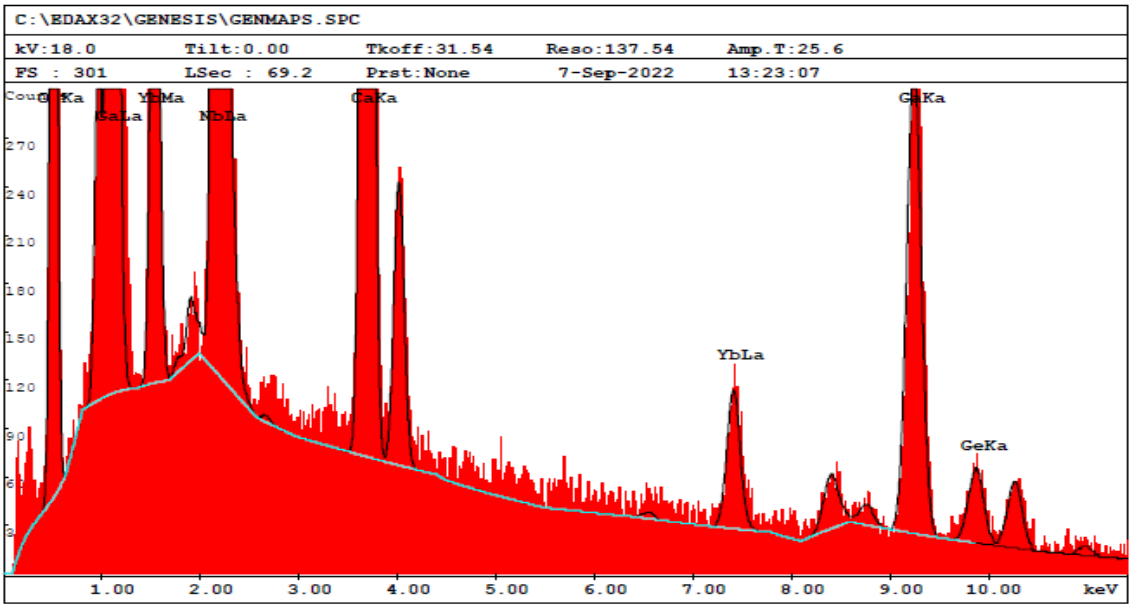

(d) 10 at% Ti-modified 8 at% Yb:CNGG

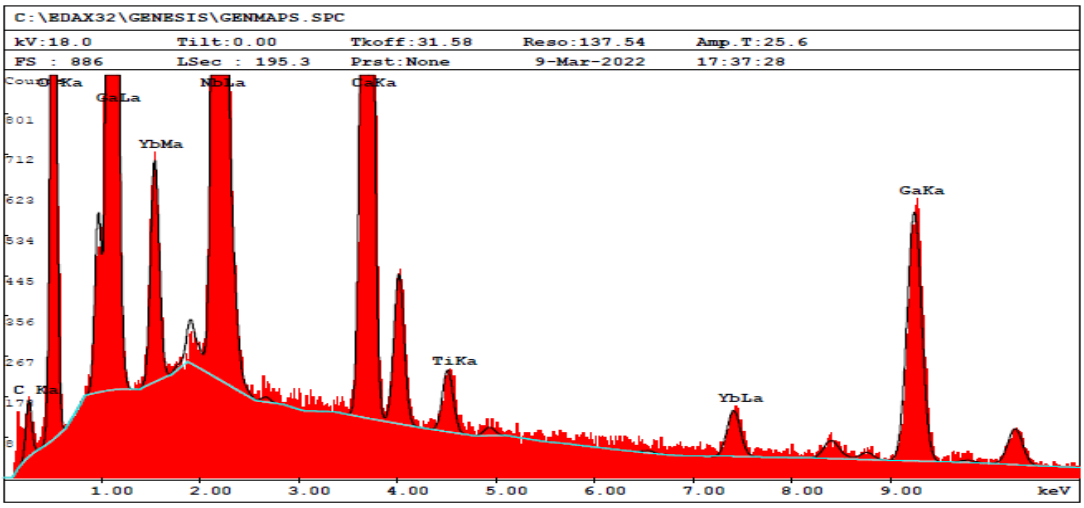

(e) 20 at% Si-modified 8 at% Yb:CNGG

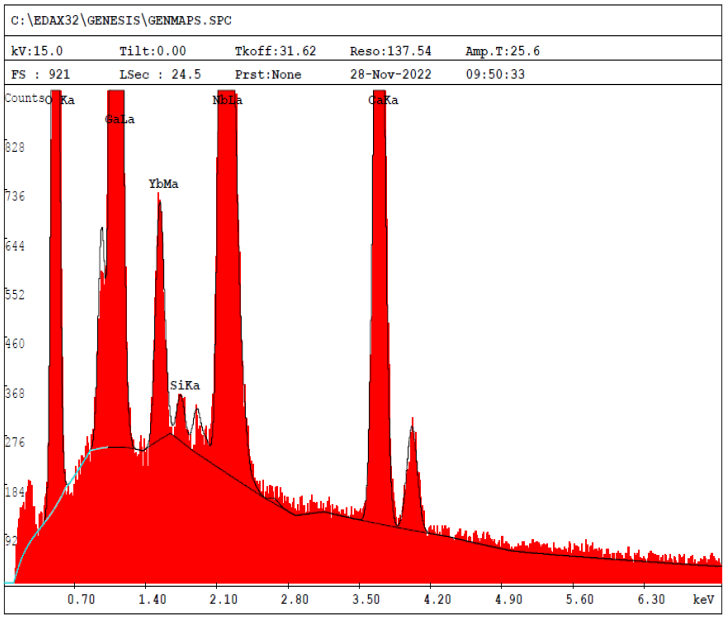

(f) 10 at% V-modified 8 at% Yb:CNGG

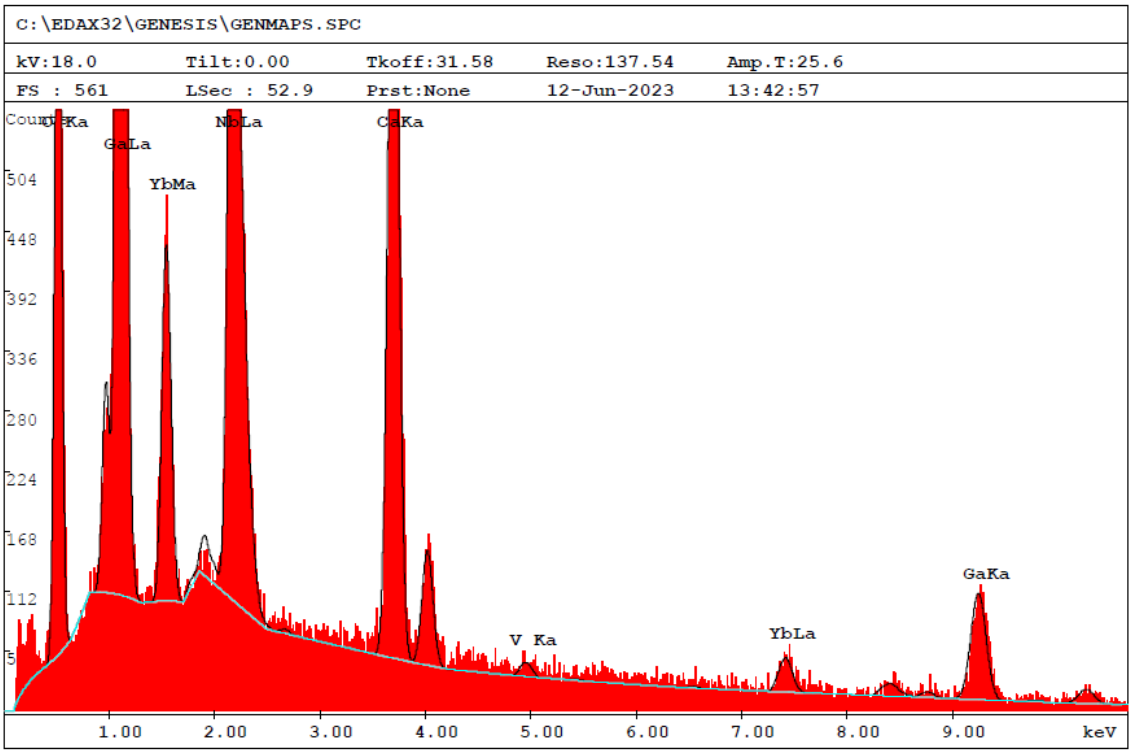

Figure ESI.7. EDX spectra of 8 at% Yb:CNGG crystals modified with different cations. (a) Unmodified. (b) 30 at% Mg^{2+}-modified. (c) 20 at% Ge^{4+}-modified. (d) 10 at% Ti^{4+}-modified. (e) 20 at% Si^{4+}-modified. (f) 10 at% V^{5+}-modified.

ESI.4. Preparation of XAS references

ESI.4.1. Czochralski growth of $Ca_3Ga_2Ge_3O_{12}$ crystal as reference of 4-fold coordinated Ge^{4+}

A single crystal garnet with nominal composition $Ca_3Ga_2Ge_3O_{12}$ (CGGG) was grown by the Czochralski method in air using a platinum crucible. The growth of this crystal was reported in several laser-related works [2,3] and its structure was reported as a model garnet phase with full occupancy of the 24*d* tetrahedral position by Ge and of the *16a* octahedral position by Ga. [4] Selective excitation of Nd^{3+} fluorescence in $Ca_3Ga_2Ge_3O_{12}$ showed the presence of Nd multisites, which was attributed to a minor occupancy by Ga^{3+} of the 24*d* tetrahedral site, but not crystallographic evidence was offered. [5]

Figure ESI.8 shows the powder XRD pattern of the grown CGGG crystals, which is identical to the previously published results.

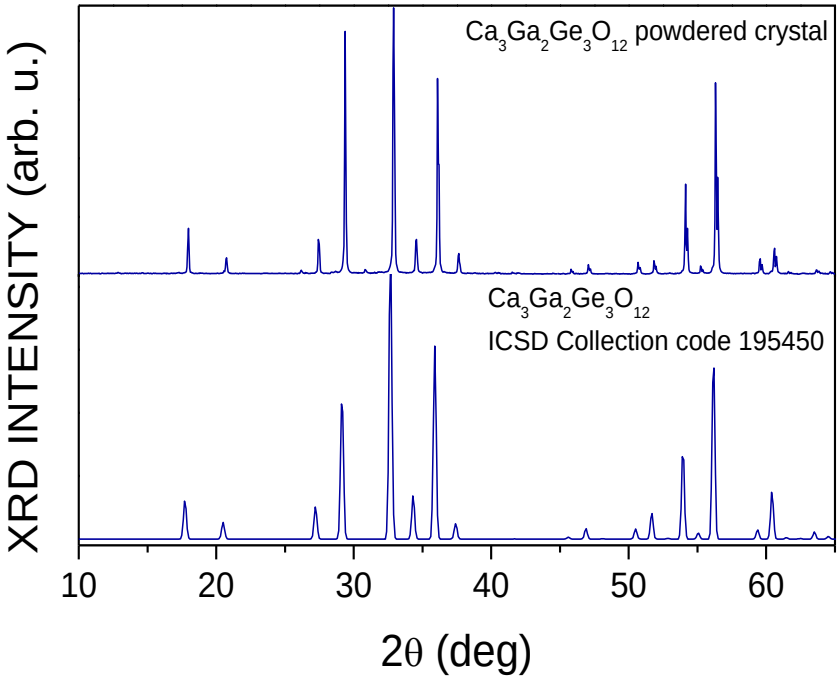

Figure ESI.8. Room temperature powder X-ray diffraction (XRD) scan of a $Ca_3Ga_2Ge_3O_{12}$ ground single crystal grown by the Czochralski method. For comparison, the reference XRD scan of the same crystal, ICSD file # 195450, [6] is shown in the bottom panel.

ESI.4.2. Spontaneous nucleation of α´-Ba_2TiO_4 as reference of 4-fold coordinated Ti^{4+}

Ba_2TiO_4 was spontaneously crystallised from a melt of a 5:5:1 molar mixture of $BaCl_2$, $BaCO_3$ and TiO_2. This mixture was put in a platinum crucible and heated in a muffle to 1340 ºC for 20 h; afterwards, the muffle was slowly cooled down to 900 ºC, and then with the furnace turned off to room temperature. It resulted in a mixture of white and dark crystals buried in a flux. The white ones are the desired α´-Ba_2TiO_4 phase. Such crystals were manually separated under low magnification (x10-20) in an optical microscope, and the collected white crystals were washed in alcohol. These crystals were manually ground in an agate mortar, and the resulting powder used as reference of Ti tetrahedral coordination in XAS measurements.

Figure ESI.9 shows the powder XRD pattern of the used α´-Ba_2TiO_4 crystal references, which is identical to the previously published results.

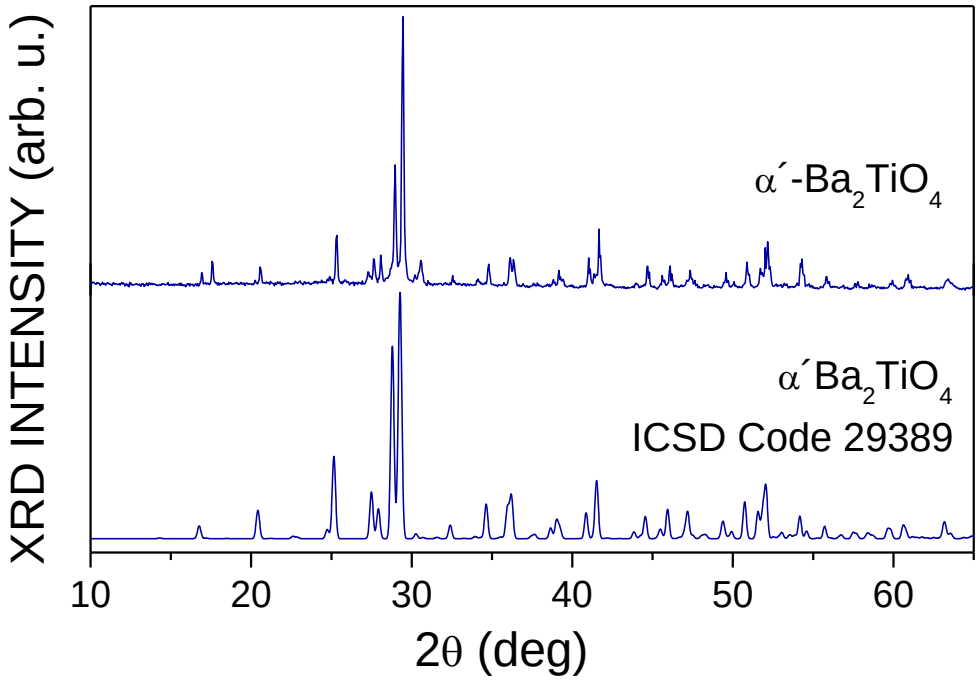

Figure ESI.9. Room temperature powder X-ray diffraction (XRD) scan of ground white crystals obtained by spontaneous nucleation upon cooling from 1340 ºC of the mixture described in the text. For comparison, the XRD scan of the orthorhombic α´-Ba_2TiO_4, ICSD file #29389, [7] is shown in the bottom panel.

ESI.4.3. Spontaneous nucleation of Y_2TiMoO_8 as reference of 4-fold coordinated Ti^{4+}

For the synthesis of 3 mmol of Y_2TiMoO_8, 2.0286 g of yttrium(III) acetate tetrahydrate, $(CH_3CO_2)_3Y\times4H_2O$ (Alfa Aesar ≥99.99 %), 0.5297 g of ammonium molybdate tetrahydrate $(NH_4)_6Mo_7O_{24}\times4H_2O$ (Sigma ≥99.0 %) and 0.2396 g of TiO_2 (Ventron GmbH, 99.9 %) were homogenised by mixing in a mortar, transferred to a platinum crucible, and heated to 900 ºC for 16 h in a muffle. After cooling, the product was ground, pressed as a pellet and heated again to 1125 ºC first for 3 h and secondly for 60 h. After further cooling and a new manual grinding, the new pellet was heated to 1165 ºC for 20 h. Figure ESI.10 shows the XRD scans of the products obtained in comparison to the $LiYb(MoO_4)_2$ scheelite phase. The Y_2TiMoO_8 scheelite phase was already formed at 1125 ºC but its crystallinity improves by further annealing at 1165 ºC.

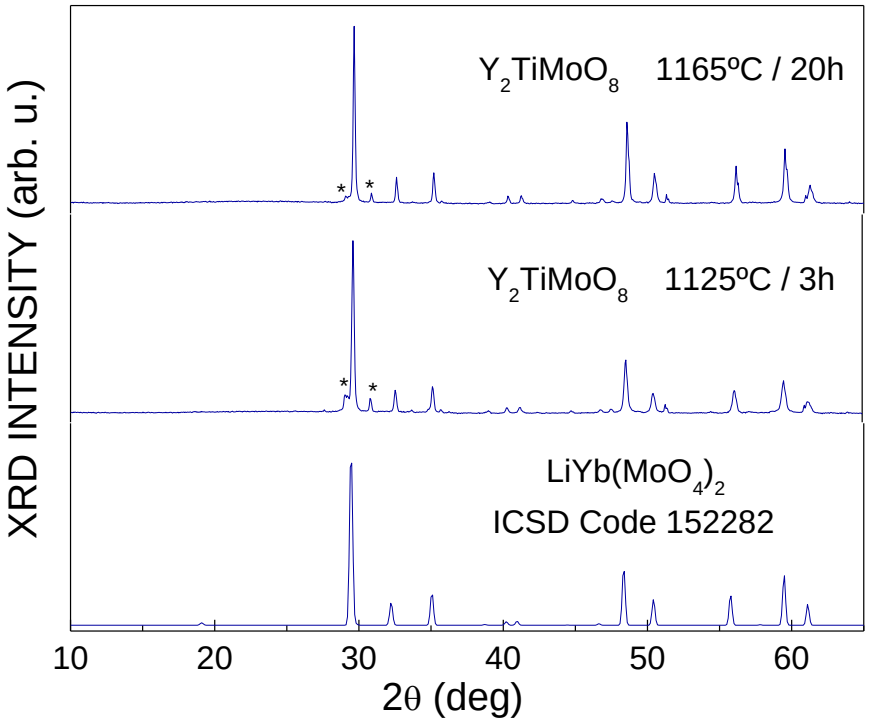

Figure ESI.10. Room temperature powder X-ray diffraction (XRD) scans of polycrystalline Y_2TiMoO_8 SSS products obtained after increasing annealing temperatures and times. For comparison, the XRD scan of the isostructural scheelite phase of $LiYb(MoO_4)_2$, ICSD file #152282, [8] is given at the bottom panel.

ESI.5. EXAFS results and data analysis

The fit of the Mg K-edge EXAFS spectrum of 30 at% Mg-modified 8 at% Yb:CNGG single crystal was performed considering Mg ions in 4-fold, 6-fold and 8-fold oxygen coordinations. Figure ESI.11 shows the fitting results. The error of these fits is represented by the R^2 parameter

$$R^2 = \sum (x_{exp} - x_{fit})^2 / N,$$

where x_{exp} and x_{fit} are the experimental and fitted values, and N is the number of fitted points.

Table ESI.3 gives the fit errors for the real and imaginary parts of the Mg K-edge $k^2\chi(k)$ weighted EXAFS FT considering the R = 1-2.7 Å radial distance range characteristic of the Mg-O bonds. EXAFS data clearly indicate that the best model for Mg coordination in CNGG corresponds to Mg^{2+} ions in the 24*d* site, with a bond distance of 1.92–1.93 Å.

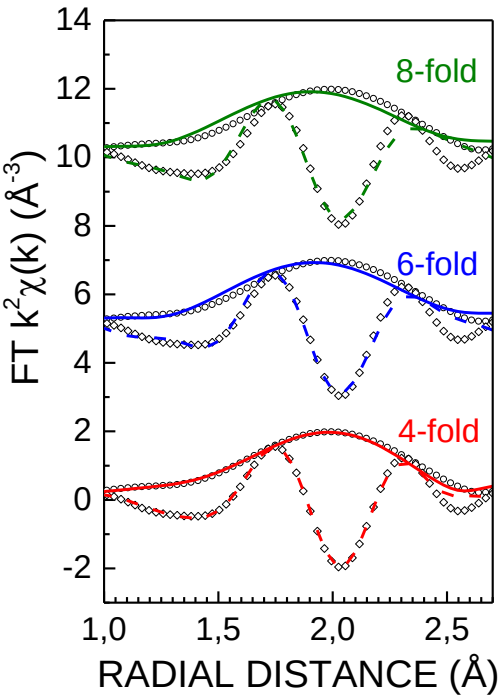

Figure ESI.11. Comparison of the experimental (symbols) and simulated (lines) real (circles and continuous lines) and imaginary (diamond and dashed lines) parts of the Fourier Transform (FT) of the Mg K-edge $k^2\chi(k)$ weighted EXAFS for 30 at% Mg-modified 8 at% Yb:CNGG assuming 4-fold (red symbols/lines), 6-fold (blue symbols/lines), and 8-fold (green symbols/lines) oxygen coordinations.

Table ESI.3. R^2 errors of the Mg K-edge $k^2\chi(k)$ weighted EXAFS FT fits considering different oxygen coordinations. (N = 59).

CN	4	6	8
R^2 real part fit	0.0061	0.0202	0.0304
R^2 imaginary part fit	0.0297	0.0590	0.0876

Tables ESI.4, ESI.5 and ESI.6 summarise the bond distances obtained from the K-edge EXAFS analyses for Mg-, Ge- and Ti-modified 8 at% Yb:CNGG crystals, respectively, and their corresponding reference compounds.

Table ESI.4. Results of the first-shell fit at the Mg K-edge. CN represents the coordination number, R is the bond distance, and σ^2 is the Debye-Waller factor.

Sample	Shell	CN	R (Å)	σ^2 (10^{-3} Å^2)
30 at% Mg-modified 8 at% Yb:CNGG	Mg-O	4	1.93(2)	3(2)

Table ESI.5. Results of the first-shell fit at the Ge K-edge. CN represents the coordination number, R is the bond distance, and σ^2 is the Debye-Waller factor. The symbol * indicates the parameters fixed in the fit.

Sample	Shell	CN	R (Å)	σ^2 (10^{-3} Å^2)
$Ca_3Ga_2Ge_3O_{12}$	Ge-O	4	1.77(1)	3.5(8)
	Ge-Ca	2	3.06(2)	2(2)
	Ge-Ga	4	3.44(2)	2(1)
	Ge-Ge	4	3.74(2)	4(3)
	Ge-Ca	4	3.78(5)	4(3)
20 at% Ge-modified 8 at% Yb:CNGG	Ge-O	4	1.79(2)	5(2)
	Ge-Ca	2	3.08(2)	6(2)
	Ge-Nb/Ga	4	3.41(5)	6(5)
	Ge-Ga	4	3.75(5)	5*
	Ge-Ca	4	3.85(7)	5*

Table ESI.6. Results of the first-shell fit at the Ti K-edge. CN represents the coordination number, R is the bond distance, and σ^2 is the Debye-Waller factor.

Sample	Shell	CN	R (Å)	σ^2 (10^{-3} Å^2)
$SrTiO_3$	Ti-O	6	1.96(2)	6(2)
	Ti-Sr	8	3.40(3)	4(2)
	Ti-Ti	6	4.00(6)	9(5)
10 at% Ti-modified 8 at% Yb:CNGG	Ti-O	6	1.96(2)	6(2)
	Ti-Ca	6	3.41(4)	8(5)
	Ti-Ga	6	3.44(3)	4(2)

ESI.6. Single crystal X-ray diffraction characterization

ESI.6.1. scXRD of 30 at% Mg-modified 8 at% Yb:CNGG crystal

Table ESI.7. Atomic coordinates (× 10^4) and equivalent isotropic displacement parameters (Å^2 ×10^3) for 30 at% Mg-modified 8 at% Yb:CNGG crystal. U(eq) is one third of the trace of the orthogonalised U^{ij} tensor.

Atom	Site	x	y	z	OF	U(eq)
Ca	24*c*	0	2500	1250	0.900(4)	9(1)
Yb	24*c*	0	2500	1250	0.060(4)	9(1)
Mg	24*c*	0	2500	1250	0.041(5)	9(1)
$\square_{DOD}$	24*c*				0	
Nb1	16*a*	0	5000	0	0.524(4)	4(1)
Ga1	16*a*	0	5000	0	0.44(1)	4(1)
Mg1	16*a*	0	5000	0	0.03(1)	4(1)
$\square_{OCT}$	16*a*				0.006	
Ga2	24*d*	0	2500	3750	0.689(4)	7(1)
Nb2	24*d*	0	2500	3750	0.07(1)	7(1)
Mg2	24*d*	0	2500	3750	0.18(1)	7(1)
$\square_{TET}$	24*d*				0.061	
O	96*h*	507(1)	3525(1)	4700(1)	1	11(1)

ESI.6.2. scXRD of 20 at% Ge-modified 8 at% Yb:CNGG crystal

Table ESI.8. Atomic coordinates (x 10^4) and equivalent isotropic displacement parameters (Å^2× 10^3) for 20 at% Ge-modified 8 at% Yb:CNGG crystal. U(eq) is one third of the trace of the orthogonalised U^{ij} tensor.

Atom	Site	x	y	z	OF	U(eq)
Ca	24*c*	0	2500	11250	0.911(2)	9(1)
Yb	24*c*	0	2500	11250	0.089(2)	9(1)
Nb1	16*a*	0	5000	10000	0.605(4)	6(1)
Ga1	16*a*	0	5000	10000	0.395(4)	6(1)
Ga2	24*d*	0	2500	8750	0.78(7)	8(1)
Ge2	24*d*	0	2500	8750	0.18(7)	8(1)
Nb2	24*d*	0	2500	8750	0.013(3)	8(1)
$\square_{TET}$	24*d*				0.027	
O	96*h*	510(1)	1488(1)	9690(1)	1	9(1)

ESI.6.3. scXRD of 10 at% Ti-modified 8 at% Yb:CNGG crystal

Table ESI.9. Atomic coordinates (x 10^4) and equivalent isotropic displacement parameters ($Å^2$ × 10^3) for 10 at% Ti-modified 8 at% Yb:CNGG crystal. U(eq) is one third of the trace of the orthogonalised U^{ij} tensor.

Atom	Site	x	y	z	OF	U(eq)
Ca	24*c*	0	2500	1250	0.936(1)	8(1)
Yb	24*c*	0	2500	1250	0.064(1)	8(1)
$□_{DOD}$	24*c*				0	
Nb1	16*a*	0	0	0	0.79(2)	6(1)
Ga1	16*a*	0	0	0	0.12(2)	6(1)
Ti	16*a*	0	0	0	0.092(4)	6(1)
$□_{OCT}$	16*a*				0.002	
Ga2	24*d*	0	2500	3750	0.917(4)	6(1)
Nb2	24*d*	0	2500	3750	0.023(4)	6(1)
$□_{TET}$	24*d*				0.06	
O	96*h*	509(1)	3525(1)	4695(1)	1	9(1)

ESI.7. Characterisation of 8 at% Yb:CNGG crystals grown in the composition limits for congruent melting

Single crystals grown with the nominal formula $Ca_{2.76}Yb_{0.24}Nb_{(1.5+1.5x)}Ga_{(3.5-2.5x)}\square_xO_{12}$ x= 0.11 and 0.14 have been grown, and their composition was characterised by EPMA. Figures ESI.12a and ESI.12b show the Ga/Nb molar ratio and the Yb composition (respect to the dodecahedral site), respectively, as a function of the distance from the growth seed. Differences found between the two grown compositions are minor, even within the uncertainty of the measurements, which shows that the initial cationic vacancy density in the precursor powders does not fully determine the final crystal composition. Environmental growth conditions and thermal history of the melt are indeed important to determine in detail the physical properties of CNGG single crystals.

Ga volatility is a known issue in the growth of Ga garnets. [9] It seems likely that the depletion of the Ga composition upon the growth time could be related to such Ga evaporation. On the other hand, the segregation coefficient of Yb is in the range 1.4-1.1, which agrees with measurements of our previous works. [10]

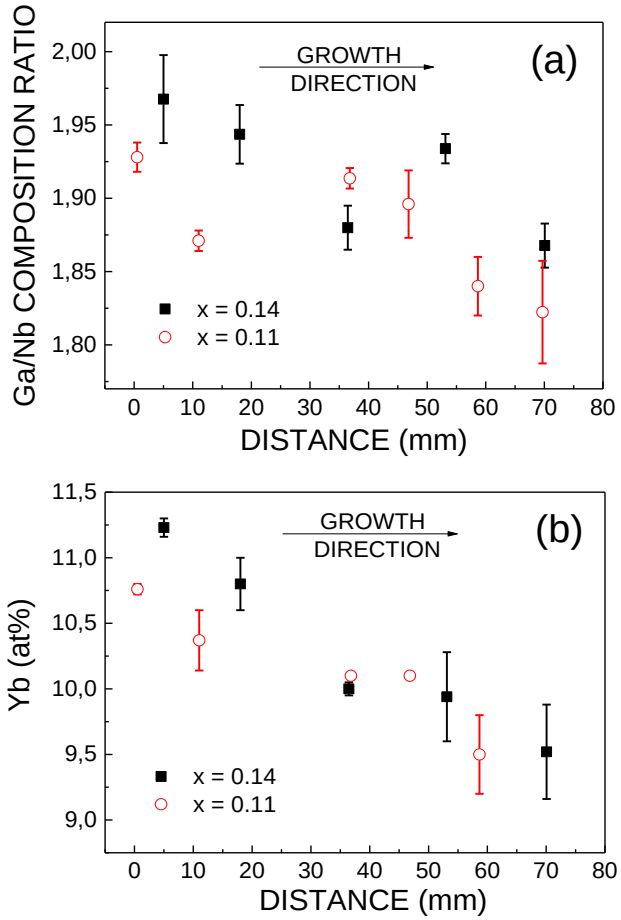

Figure ESI.12. Composition of 8 at% Yb doped $Ca_3Nb_{(1.5+1.5x)}Ga_{(3.5-2.5x)}\square_xO_{12}$, x = 0.11 and 0.14, single crystals for different crystal axial positions from the seed (zero distance). (a) Ratio of the Ga and Nb compositions. (b) Atomic Yb composition referred to the dodecahedral site.

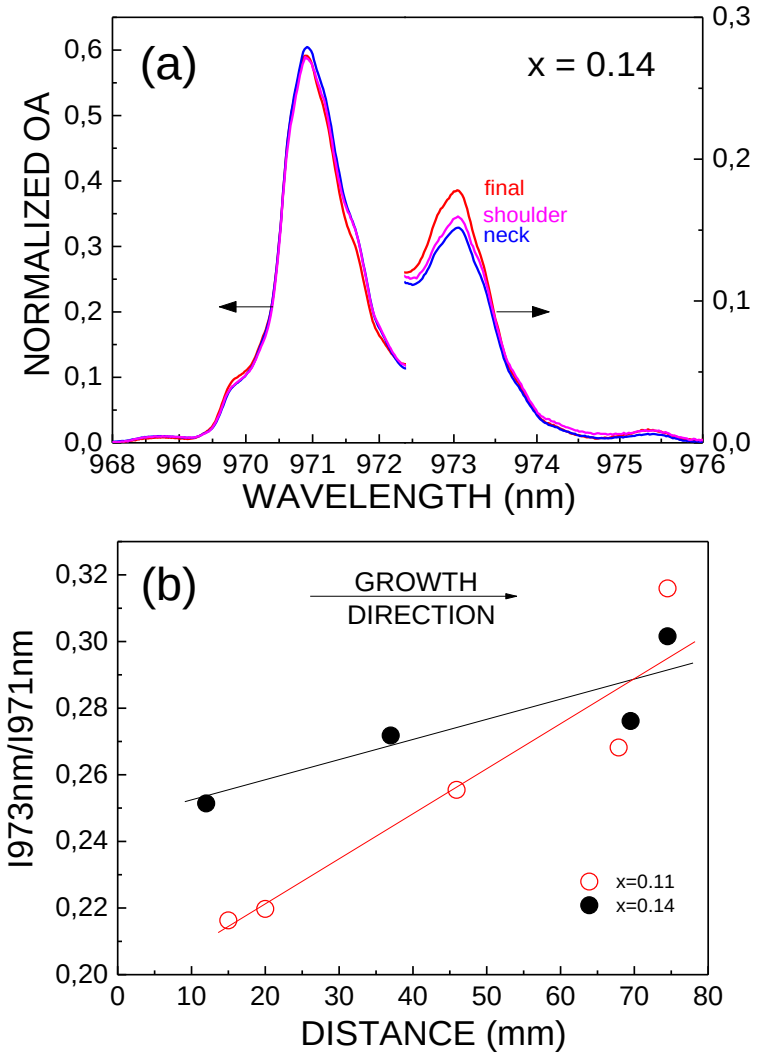

Figure ESI.13. (a) Evolution of the T= 6 K OA of Yb^{3+} in 8 at% Yb doped $Ca_3Nb_{(1.5+1.5x)}Ga_{(3.5-2.5x)}\square_xO_{12}$, x = 0.14, single crystal garnet with the distance from the growth seed (increasing growth time). To ease the comparison, the spectra are normalised to unit area. Each spectrum is the average of 15 acquisitions with a spectral resolution of 0.1 nm. (b) OA peak intensity ratio at λ = 973 nm and λ = 971 nm for x = 0.11 (open red symbols) and x = 0.14 (full black symbols) crystals at several distances from the seed. The lines are just a visual help.

The study of the 0→0´ Yb^{3+} OA measured at T = 6 K in samples sliced at different crystal axial distances (the seed position is considered as zero distance, and distance increases with the growth time) reveals that the intensity of the absorption peak at λ = 973 nm increases as the crystal growth progresses, see Figure ESI.13. Since Ga evaporation is suggested by the Ga/Nb composition decrease upon growth time, see Figure ESI.12a, it is likely that the crystal becomes enriched in Nb^{5+} as it grows. Thus cationic vacancies are created for charge compensation, which is consistent with the increase of the OA intensity at λ = 973 nm, associated in our model to the presence of 24*d* tetrahedral vacancies near Yb^{3+}.

ESI.8. Low temperature (T= 6K) OA of Ge-, Si-, or V-modified 8 at% Yb:CNGG SSS products and single crystals

ESI.8.1. Ge^{4+}

The 0→0´ Yb^{3+} OA measured at T = 6 K in CNGG crystals modified with 20 at% Ge presents an overlapped band in the high-energy wing of the main band observed in all cases at λ = 971.1 nm. The individual contribution of this band characteristic of the Ge presence is disclosed by a gaussian decomposition of the spectra shown in Figure ESI.14. Table ESI.10 summarises the parameters (intensity, peak position and bandwidth) of the three component bands used in the fit. The new band peaks at λ = 969.6 nm, i.e at a higher energy than any other contribution of all studied cases, with Ge^{4+} being the largest charge introduced by foreign cations.

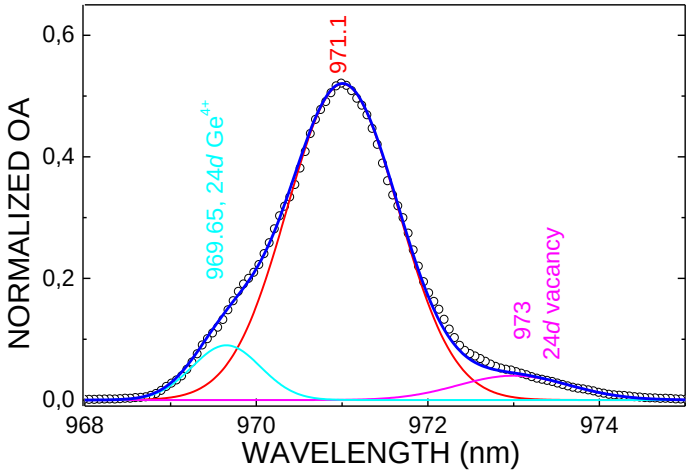

Figure ESI.14. Gaussian deconvolution of the 0→0´ Yb^{3+} optical absorption (OA) of 20 at% Ge-modified 8 at% Yb:CNGG single crystal measured at T = 6 K. The spectrum has been normalised to unit area.

Table ESI.10. Parameters of the gaussian band decomposition of the T = 6 K 0→0´ Yb^{3+} OA of 20 at% Ge modified 8 at% Yb:CNGG.

Band peak position (cm^{-1}/nm)	Band intensity	Bandwidth (cm^{-1})	Asignment
10313 / 969.6	0.09	6	Ge^{4+} - Yb^{3+} - Ga^{3+}
10298.6 / 971.1	0.52	9.8	Ga^{3+} - Yb^{3+} - Ga^{3+}
10277.5 / 973	0.04	9.7	$\square_{TET}$ - Yb^{3+} - Ga^{3+}

ESI.8.2. Si^{4+}

10 at% (with regards to Ga) Si-modified 8 at% Yb:CNGG powders were obtained by SSS. The 0→0´ Yb^{3+} electronic transition was determined through the measurement of the photoluminescence excitation spectra at T = 6 K. Figure ESI.15 shows the obtained result in comparison to the OA of 8 at% Yb:CNGG measured at T = 6 K. In addition to broad bands, characteristic of Yb:CNGG, another overlapped band, much narrower and intense, appears at λ = 972.2 nm indicating the presence of multiple crystalline phases in the powder. Nevertheless, the high-energy wing of the λ = 971 nm band shows an increase of the OA similar to that obtained in Ge^{4+}-modified single crystals. So we attempted the Czochralski growth of Si-modified Yb:CNGG single crystals.

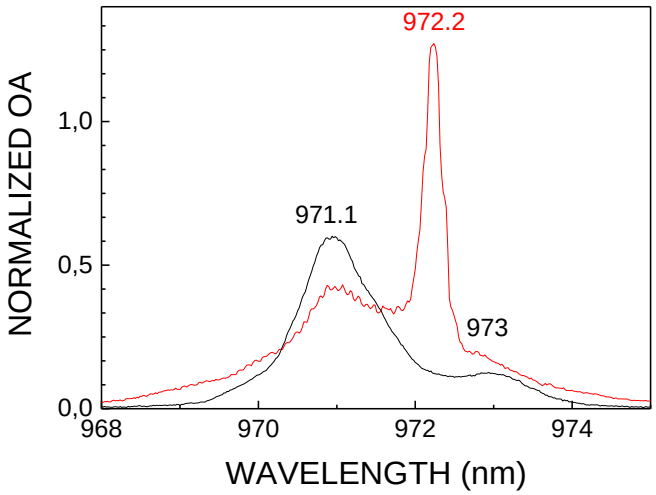

Figure ESI.15. Comparison of the T = 6 K excitation spectrum of 10 at% Si-modified 8 at% Yb:CNGG powders obtained by SSS (red line, λ_{EMI} = 1020 nm) with the T = 6 K OA of 8 at% Yb:CNGG normalised to unit area.

Single crystals with three Si doping levels with regard to Ga, 5 at% Si+ 8 at% Yb:CNGG, 10 at% Si+8 at% Yb:CNGG and 20 at% Si+8 at% Yb:CNGG were grown. The EDX results presented in section ESI.3, see Figure ESI.7e, show that the Si incorporation to the solids obtained is small and some areas are strongly Ga deficient, suggesting the presence of second phases. Powder XRD studies of these crystals shown in Figure ESI.3 evidence the presence of second crystalline phases. Despite the poor optical quality of these crystals, they have some transparent areas that we used to monitor the OA of Yb^{3+}, see Figure ESI.3c.

Figure ESI.16 shows the results for the two largest Si compositions grown. The recorded spectra are basically equal to that of Si-free 8 at% Yb:CNGG. The small Si incorporation into the Yb:CNGG phase is the most likely reason for these results. Like in other CNGG crystals studied, the intensity of the λ = 973 nm OA is slightly larger at the crystal end than at the beginning; see Figure ESI.16a.

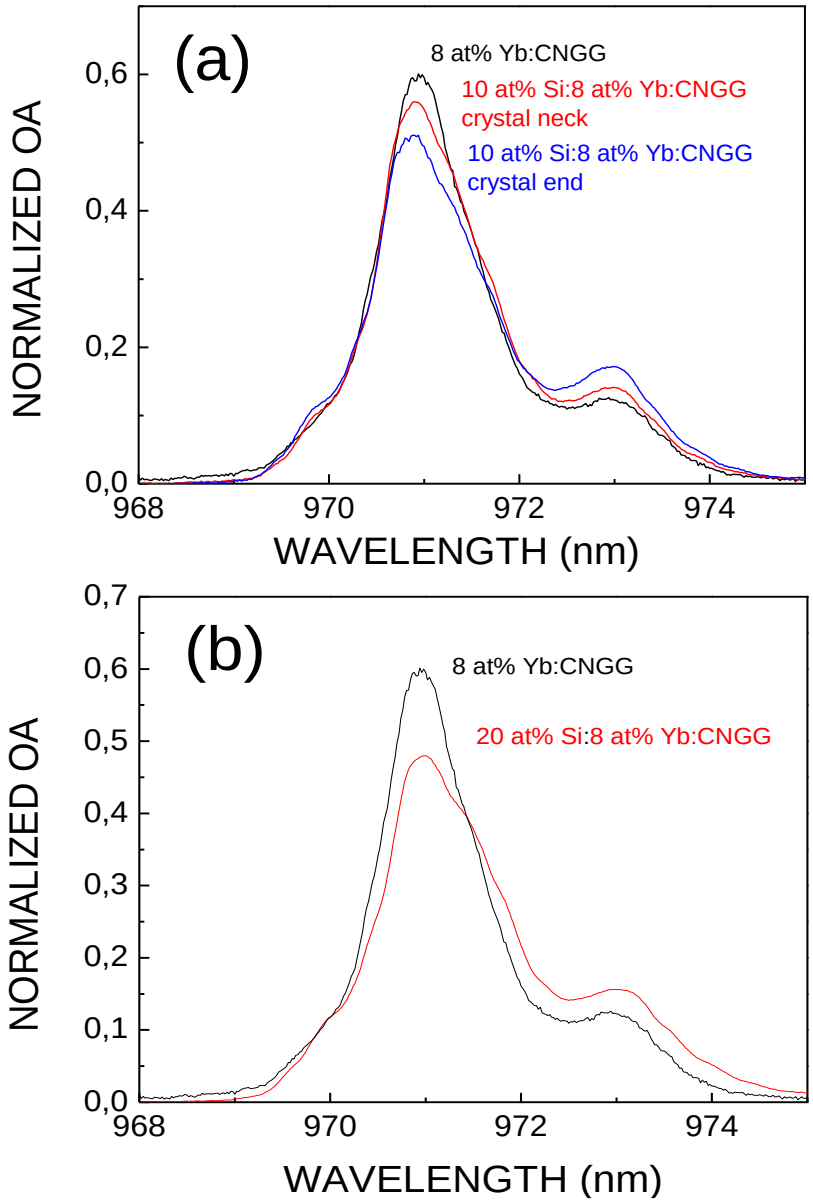

Figure ESI.16. Comparison of the 0→0´ Yb^{3+} OA measured at T = 6 K of Si-modified 8 at% Yb:CNGG (red lines) and 8 at% Yb:CNGG (black line) single crystals. All spectra are normalised to unit area. (a) 10 at% Si. (b) 20 at% Si.

ESI.8.3. V^{5+}

V^{5+} have been found in the tetrahedral 24*d* garnet site, either by full occupancy of this position, like in $NaCa_2M_2V_3O_{12}$ (M= Ni, Mg or V), [11] and $LiCa_3MV_3O_{12}$ (M= Zn, Mg) [12,13] or by sharing this position with Ge and Si. [14] Vanadium is also found in octahedral 16*a* garnet sites but with trivalent oxidation state, V^{3+}, see Figure ESI.1a. However, the case of CNGG is rather peculiar because Nb^{5+} is the main population of the 16*a* site, thus a priori, it could be displaced by V^{5+} with not very large ionic radii mismatch, $\Delta r \approx 15\%$, leading to a unique case of V^{5+} 16*a* centre in garnets.

To our knowledge, the presence of vanadium in CNGG has never been reported; thus, we first examined the phases present in SSS powders. For this purpose the desired nominal amount of V in 8 at% Yb:CNGG was discounted from the total Ga composition to ease its incorporation into the tetrahedral 24*d* site. The XRD study of SSS powders of V-modified 8 at% Yb:CNGG shows that up to 10 at% substitution of Ga by V yields exclusively the garnet phase; see Figure ESI.6. Above it other XRD reflections corresponding to foreign phases are observed.

We first examined the spectroscopic properties of the SSS powders. Figure ESI.17a shows a comparison of the excitation spectrum corresponding to 10 at% V-modified 8 at% Yb:CNGG polycrystalline SSS powder with the corresponding optical absorption spectra of 8 at% Yb:CNGG single crystal. To ease the comparison, both spectra have been normalized to unit area. According to our previous assignment of the λ = 973 nm OA band observed at T = 6 K to the presence of tetrahedral vacancies neighbouring Yb, it seems most likely that V does not fill these vacancies, which does not exclude some 24*d* V^{5+} presence. Further, the Yb^{3+} excitation spectra of 10 at% V-modified 8 at% Yb:CNGG polycrystalline powders show new features on the high energy wing of the main band at λ < 970 nm, that could be compatible with the presence of V^{5+} in the tetrahedral 24*d* garnet site leading to a Yb^{3+} band similar to the Ge^{4+} case. However, these spectral changes upon V incorporation in the garnet structure are not found in the 15 at% V-modified 8 at% Yb:CNGG grown single crystals; see Figure ESI.17b. The reason for that is that V does not incorporate from the melt into the solid phase upon crystal growth as demonstrated by the EDX, see Figure ESI.7f.

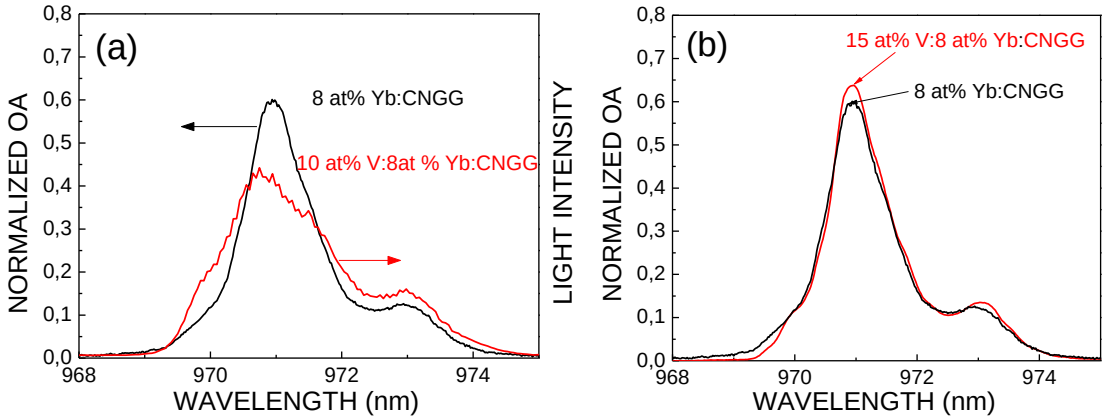

Figure ESI.17. Comparison of the 0→0′ Yb^{3+} optical absorption (OA) of V-modified 8 at% Yb:CNGG products (red line) with that of 8 at% Yb:CNGG single crystal (black line) measured at T = 6 K. (a) Excitation spectrum of 10 at% V-modified 8 at% Yb:CNGG SSS powder. λ_{EMI} = 1020 nm. (b) OA of 15 at% V-modified 8 at% Yb:CNGG single crystal. All spectra have been normalised to unit area.

References

[1] A. A. Kaminskii, E. L. Belokoneva, A. V. Butashin, K. Kurbanov, A. A. Markosyan, B. V. Mill', O. K. Nikol'skaya and S. E. Sarkisov, *Izvestiya Akademii Nauk SSSR, Neorganicheskie Materialy,* 1986, **22**, 1061-1971.

[2] A. A. Kaminskii, B. V. Mill and A. V. Butashin, *Phys. St. Sol. A-Appl. Res.* 1983, **78** (2) , 723-732,. https://doi.org/10.1002/pssa.2210780242

[3] P. Peicong, T. Yamazaki, A. Sugimoto, K. Yamagishi and H. Takei, Jap. J. Appl. Phys. Part 1 1995, **34**, 515-516. https://doi.org/10.1143/JJAP.34.515

[4] C. Liu, Z. Xia, M. S. Molokeev and Q. Liu, *J. Am. Ceram. Soc.*, 2015, **98**, 1870–1876. https://doi.org/10.1111/jace.13553

[5] U. Caldiño, M. Voda, F. Jaque, J. García- Solé and A. A. Kaminskii, *Chem. Phys. Lett.* 1993, **213**, 84-88. https://doi.org/10.1016/0009-2614(93)85422-K

[6] C. Liu, Z. Xia, M. S. Molokeev and Q. Liu, *J. Am. Ceram. Soc.,* 2015, **98**, 1870–1876. https://doi.org/10.1111/jace.13553.

[7] J. R. Günter and G. B. Jameson, *Acta Cryst.* 1984, **C40**, 207-210. https://doi.org/10.1107/S0108270184003619

[8] V. Volkov, C. Cascales, A. Kling and C. Zaldo, *Chem. Mater*. 2005, *17*, 291–300. https://doi.org/10.1021/cm049095k

[9] V. Kochurikhin, K. Kamada, K. J. Kim, M. Ivanov, L. Gushchina, Y. Shoji, M. Yoshino and A. Yoshikawa, *J. Cryst. Growth* 2020, **531**, 125384,. https://doi.org/10.1016/j.jcrysgro.2019.125384

[10] J. O. Álvarez-Pérez, J. M. Cano-Torres, A. Ruiz, M. D. Serrano, C. Cascales and C. Zaldo, *J. Mater. Chem. C*, 2021, **9**, 6945-6946. https://doi.org/10.1039/D0TC05718E

[11] K. Iishim and J. Utsumi, *J. Cryst. Growth* 2006, **291**, 436-441. https://doi.org/10.1016/j.jcrysgro.2006.03.011

[12] T. Hasegawa, Y. Abe, A. Koizumi and T. Ueda, K. Toda, *Inorg. Chem* 2018, **57**, 857-866. http://doi-org/10.1021/acs.inorgchem.7b02820

[13] G. Bayer, *J. Am. Ceram. Soc.* 1965, **48**, 600-600. https://doi.org/10.1111/j.1151-2916.1965.tb14681.x

[14] B. V. Mill, G. Ronniger and Y. K. Kabalov, *Russ. J. Inorg. Comp.* 2014, 59, 1208-1213. https://doi.org/10.1134/S0036023614110151